Variability of surface gravity wave field over a realistic cyclonic eddy

Gwendal Marechal[1,*] and Charly de Marez[1,*]

[1]Univ. Brest, CNRS, Ifremer, IRD, Laboratoire d'Océanographie Physique et Spatiale, Brest, France
[*]These authors contributed equally to this work.

Correspondence: gwendal.marechal@ifremer.fr

Abstract. Recent altimeters and numerical studies have shown that surface gravity waves interact strongly with small-scale open ocean currents, and subsequently modify the significant wave height, wave frequency, and wave direction. In the present paper we investigate the interactions of surface gravity waves with a large and isolated realistic cyclonic eddy. This eddy is subject to instabilities leading to the generation of specific features both at mesoscale and submesoscale. We use the WAVE-WATCH III framework to force surface gravity waves in the eddy before and after instabilities appeared. Our findings show that the spatial variability of wave direction, wave mean period and significant wave height is very sensitive to the presence of submesoscale structures resulting from the eddy destabilisation. As well as small-scale current structures, the intrinsic frequency of incident waves is key in the wave response of the current modulation, especially for wave direction. Our findings also suggest that surface current gradients could be approached thanks to significant wave height gradients measurements until very small spatial resolution. However it is difficult to have information on the phase of those current gradients due to the non-local effects of currents on waves.

1 Introduction

The ubiquity of mesoscale (10-100 km) and submesoscale (1-10 km) eddies, fronts, and filaments at the superficial layer of the ocean induces a strong variability in the wave field generated by wind (waves): waves-current interactions result in a change of significant wave height (H_s), frequency, and direction (Phillips (1977) and Mei (1989)). From these modulations, it has been proved recently, thanks to both field measurements and numerical simulations, that the effects of currents on waves induce strong regional inhomogeneities of the wave field (Romero et al., 2017, 2020). In particular, Ardhuin et al. (2017) showed thanks to realistic numerical simulations that the H_s variability is closely linked to surface Kinetic Energy (KE) at mesoscale. Quilfen et al. (2018); Quilfen and Chapron (2019) used high resolution H_s measurements from altimetry to highlight the close link between current gradients (∇U) and significant wave height gradients (∇H_s). Villas Bôas and Young (2020) proved, in the absence of wave dissipation and wind momentum input, that the gradients of the wave direction induced by current is necessarily induced by the solenoidal component of the surface currents (vorticity). Finally, Villas Bôas et al. (2020), under the same assumptions, emphasized the narrow link between the surface vorticity of the flow and the ∇H_s. Surface currents seem to increase the deep-water breaking wave probability (Romero et al., 2017, 2020). Wave breaking at the air-sea interface is the major source of momentum and heat exchange between waves and currents (Cavaleri et al., 2012) or gas and sea spray

production (Monahan et al., 1986; Bruch et al., 2021). That is why surface mesoscale and submesoscale currents, through their interactions with the wave field, have a significant impact on air-sea fluxes (momentum, gas, heat, sea-spray, ...).

In the ocean and particularly in western boundary currents, eddies are ubiquitous from mesoscale to submesoscale (Chelton et al., 2007, 2011; Gula et al., 2015b; McWilliams, 2016; Rocha et al., 2016). The interaction between eddy field and waves is thus of primary importance for the global distribution of wave properties. In the present study, we analyse numerically the effect of an isolated realistic eddy on the wave properties (H_s, mean period, and direction). Former similar works have been already performed, but only for idealized eddy cases (Gaussian profiles, see Gallet and Young (2014); Mapp et al. (1985); Mathiesen (1987); White and Fornberg (1998); Holthuijsen and Tolman (1991)). However, the structure of eddies in the ocean can strongly differ from textbook analytical idealized profiles (Le Vu et al., 2018; de Marez et al., 2019), making the study of waves-Gaussian eddy an unrealistic framework. Indeed, the instabilities occurring in a large and isolated eddy result in the strong production of energy in the oceanic submesoscales range (Hua et al., 2013; de Marez et al., 2020b) which would interact strongly with waves. Furthermore, most of the previous studies solely focused on the refraction induced by an eddy without discussing on the modulation of wave parameters (H_s or mean wave period, Gallet and Young (2014); Mapp et al. (1985); White and Fornberg (1998)). Here, our goal is to investigate the long-term mean effects of an isolated cyclonic eddy with a realistic shape (highly dynamic at meso- and submesoscale) on the wave properties. We demonstrate that wave field characteristics are strongly modified by the presence of the eddy and that the variabilities are more important as the eddy field is multi-scale dynamic. In a real ocean, the resulting deviation of the waves from the great circle path due to eddy-induced refraction are thus certainly underestimated when eddies are considered as gaussian (Gallet and Young, 2014; Smit and Janssen, 2019) as well as extreme wave height waves in eddy that can be found in the vicinity of main branches of western boundary currents, e.g in the Gulf-Stream (Holthuijsen and Tolman, 1991). Also, the estimated ocean circulation from altimeters measurements are affected by noise correlated to the H_s. Some proposed methods to remove the contribution of waves in altimeters measurements assume that the wave field is sufficiently smooth under 200 km (Sandwell and Smith, 2005). Focus on H_s variability over a realistic eddy field pattern (more realistic than a gaussian eddy) will reveal very sharp wave parameter gradients thus making the assumption that wave field homogeneous at the scale of hundred kilometers not acceptable. Finally, previous works showed that wave characteristic can be inverted to infer surface currents intensity (Huang et al., 1972; Sheres et al., 1985) or more recently Villas Bôas et al. (2020). The last study showed that sharp emerging ∇H_s can be inverted to infer the ∇U that have generated them. In the same framework of Villas Bôas et al. (2020) we will show that the amplitude of ∇U can be approached by inverting the variabilities of the wave field induced by the eddy field. Reconstruct the ∇U field would be fruitful for a wide range of applications (search and rescue, plastic debris monitoring, biological activities or short-term wave forecast).

The manuscript is organised as follows. In section 2, we introduced the eddy structure used in the study, based on the work of de Marez et al. (2020b), and the numerical framework WAVEWATCH III (The WAVEWATCH III $^{\circledR}$ Development Group, 2016) without source terms. In section 3, we present the results of the numerical experiments. In section 4, we discuss on how significant wave height and current gradients are coupled. In section 5 we investigate quickly the effects of nonlinear wave-wave interactions on the intensity of the wave parameter gradients. Limits and perspectives of this present work close the manuscript.

2 Method

2.1 A cyclonic eddy from in-situ measurements

To study the wave propagation through an eddy field, we used the outputs of the simulation performed by de Marez et al. (2020b). In this study, authors performed idealized simulations, using the Coastal and Regional Ocean COmmunity model, CROCO (Shchepetkin and McWilliams, 2005), that solves the hydrostatic primitive equations (PE) for the velocity $\mathbf{u} = (u, v, w)$, temperature T, and salinity S, using a full equation of state for seawater (Shchepetkin and McWilliams, 2011). The spatial resolutions are chosen to accurately resolve both the frontal dynamics and the forward energy cascade at the surface. The simulation is initialised with a composite cyclonic eddy as revealed by Argo floats in the northern Arabian Sea (details of the composite extraction are fully described in de Marez et al. (2019)). The eddy is intensified at the surface, but has a deep-reaching influence down to about 1000 m depth. Its initial horizontal shape corresponds to a shielded vorticity monopole: a positive core of vorticity and a shield of negative vorticity (Fig. 1(a)). Its radius, $R = 100$ km, is large compared to the mean regional Rossby radius R_D (47 km, see Chelton et al. (1998)). It is a mesoscale eddy. In the following, mentions to "submesoscale" refers to features and processes occurring at scales that are small compared to Rossby deformation radius (*i.e.* $Bu > 1$ with $Bu = \frac{R_D^2}{L^2}$). de Marez et al. (2020b) observed that the eddy is unstable with respect to a mixed barotropic/baroclinic instability. The latter deforms the eddy, which eventually evolves into a tripole after about 4 months of simulation. Sharp fronts are subsequently generated in the surface mixed layer at the edge of the tripole. These fronts then become unstable, and this generates submesoscale cyclones and filaments. Near these fronts, diapycnal mixing occurs, causing the potential vorticity to change sign locally, and symmetric instability to develop in the core of the cyclonic eddy. Despite the instabilities, the eddy is not destroyed and remains a large-scale coherent structure for one year of simulation. A full description of instability processes can be found in de Marez et al. (2020b). Snapshots of the current velocity and vorticity of the fully developed eddy field after 210 days of simulation are represented in Fig. 1b and d respectively. The main core of the cyclone is surrounded by filaments, submesoscale eddies and fronts, that lead to sharp vorticity gradients. This vorticity field is far from the usual idealised representation of eddies often considered in the literature, and is closer to reality (see *e.g.* Fig. 1 in Lévy et al. (2018) for an example of a realistic turbulent field above mesoscale eddies).

For the purpose of the present study, we consider the surface velocity fields (the simulated level closest to the ocean surface) from the simulation outputs described above. We use the initial state that represents the eddy before instabilities occur (Fig. 1(a)), and the state after 210 days of simulation, in which submesoscale features have been generated by the spontaneous instability of the eddy (Fig. 1(b)). At 210 days all instabilities have occurred (mixed barotropic/baroclinic instabilities). After 210 days the eddy field starts to dissipate making some small-scales features disappear (de Marez et al., 2020b). Please notice that the use of strictly 2D surface current is an approximation of what happen in the nature. In reality, waves feel the effects of an "average current" integrated over a certain depth along the first meters of the water column. This depth depends on the wavelength of the waves (Kirby and Chen, 1989).
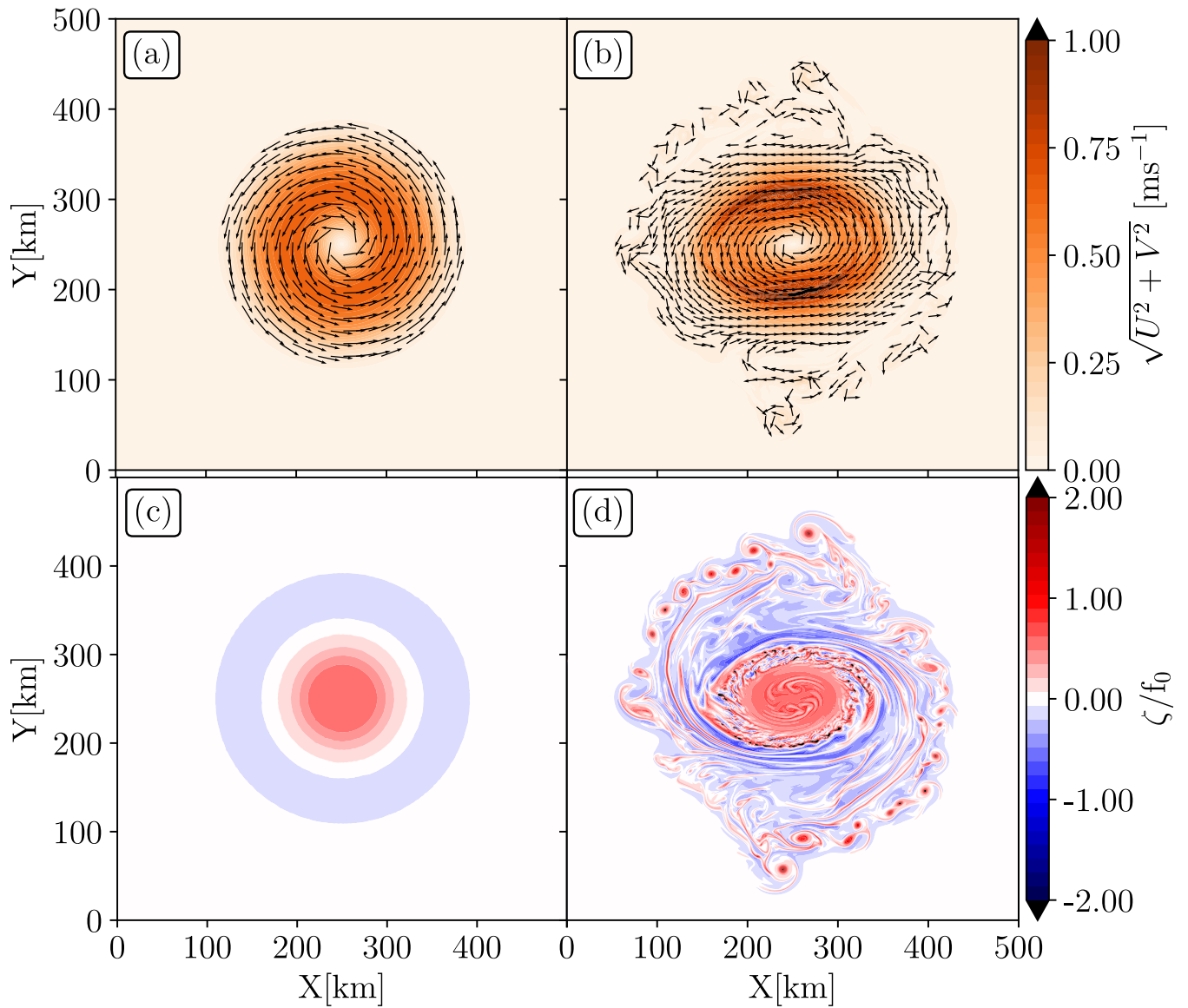
Figure 1. Surface currents intensity and direction for the initial/gaussian eddy (panel (a)) and after 210 days of destabilization (panel (b)). Their associated normalized relative vorticity ($\zeta = \partial_x V - \partial_y U$) are given in panel (c) and (d). The Coriolis parameter is kept constant in the simulations: $f_0 = 5.2\,10^{-5}\,\mathrm{s}^{-1}$. The original zonal and meridional velocities (de Marez et al., 2020b) have been here multiplied by two.

2.2 The wave model

To describe the dynamic of waves over the eddy described above, we use the WAVEWATCH III framework (The WAVE-WATCH III ® Development Group, 2016) forced both by the initial state of the eddy (gaussian shape, Fig.1a,c) and the fully developed eddy (Fig.1b,d). The model integrates wave action equation

$$\partial_t N(\sigma,\theta) + \nabla.(\dot{x}N(\sigma,\theta)) + \partial_k(\dot{k}N(\sigma,\theta)) + \partial_\theta(\dot{\theta}N(\sigma,\theta)) = S, \tag{1}$$

where $N(\sigma,\theta)$ is the wave action ($N(\sigma,\theta) = \frac{E(\sigma,\theta)}{\sigma}$, with $E(\sigma,\theta)$ the two dimensional wave energy spectrum), θ is the wave direction of propagation, $\dot{x}$ is the wave action advection velocity (equal to the sum of the wave group and the surface current velocity), $\dot{k}$ and $\dot{\theta}$ are the wave advection velocities in the spectral space The expressions of $\dot{k}$ and $\dot{\theta}$ are developed from wave ray equations (Eq.3) and are fully given in (Phillips, 1977; Benetazzo et al., 2013; Ardhuin et al., 2017). The right hand side of Eq. (1) is the sum of the source terms describing the wind energy input, the dissipation due to wave breaking and bottom friction, and the nonlinear energy exchange between waves.

In a current field, it is necessary to consider a non-Galilean frame of coordinate (moving frame of reference). The waves dispersion relationship is thus impacted because the current induces a Doppler shift on the wave frequency (Eq.(2)),

$$\omega = \sigma + \mathbf{k}.\mathbf{u}. \tag{2}$$

The wave ray equation is also modified,

$$\partial_t\mathbf{k} = \partial_\mathbf{x}\omega. \tag{3}$$

ω is the absolute frequency, $\mathbf{k}$ the wavenumber vector, $\mathbf{u}$ the surface current vector, σ the intrinsic wave frequency equal to $\sqrt{gk}$ in deep water (where water depth is largely greater than wave wavelength, here k is a scalar) and g is the gravity acceleration. Bold characters refer to vector notation all along this manuscript. For this study we consider waves already well developed, far from their generation areas, propagating in the current field without any source term (no dissipation, no nonlinear exchange between waves, and no wind input, i.e. the right hand side of Eq.(1) is equal to 0). The aim of the current study is to investigate, in a very idealized case, how long waves properties can be modified by an eddy field more realistic than an isolated and gaussian eddy. In a more realistic framework, the waves steepness modified by the current or due to non initial waves-waves interactions would trigger local wave breaking as observed in Romero et al. (2017). Also wind input would generate higher frequency waves which will also interact with the eddy field. In a fully coupled simulation, the currents itself would be modified due to the presence of the waves at the air-sea interface.

Throughout this manuscript we discuss the evolution of the H_s and the mean wave period weighted on the low frequency part of the wave spectrum ($T_{m0,-1}$), known as "bulk" quantities. We called them "bulk" because they are integrated over the wave energy spectrum $E(\sigma,\theta)$.

They are defined as

$$H_s = 4\sqrt{\int_\theta \int_\sigma E(\sigma,\theta)\,d\sigma d\theta}, \tag{4}$$

and

125 $$T_{m0,-1} = \frac{1}{\int_\theta \int_\sigma E(\sigma,\theta)d\sigma d\theta} \int_\theta \int_\sigma \sigma^{-1} E(\sigma,\theta)d\sigma d\theta. \tag{5}$$

The evolution of the wave peak direction (θ_p, θ where E(σ,θ) is maximum) has been also studied. The performance of the wave model used here has already been discussed in boundary currents systems such as the Gulf Stream, Drake Passage and Agulhas current, especially concerning the H$_s$ estimation (Marechal and Ardhuin, 2021; Ardhuin et al., 2017). In those previous studies, wind forcing, waves dissipation, and nonlinear wave-wave interactions have been taken into account.

130 We initialized simulations with waves that are propagating from the left boundary of a 500×500 km Cartesian domain, with a resolution of 500 m both in horizontal and vertical directions. The right boundary is open. The initialization is done with a narrow-banded wave spectra gaussian in frequency centered at varying peak frequencies, f_p=0.1428 Hz, 0.097 Hz, and 0.0602 Hz. The spectral energy spectrum has a frequency spreading of 0.03 Hz around the peak frequency and H$_s = 1$ m. The frequencies have been chosen to correspond to the mean periods used in the work of Villas Bôas et al. (2020) (7 s,

135 10.3 s, and 16.6 s). Waves are generated at the left boundary, from spectra described above, every hour. The initial direction of waves is 270°$^]$. The direction convention follow the meteorological convention such that 270° waves are coming from the left and 0° waves are coming from the top of the domain. The wave field reaches a stationary state after 09:15, 08:45, and 07:30 of simulation for initializations of T$_p$=7 s, T$_p$=10.3 s, and T$_p$=16.6 s, respectively, we recall that source terms have been removed and the current field assumed stationary. The wave model global time step is 12 s, the spatial advection time step is

140 4 s, and the spectral time step is 1 s. The model provide outputs every fifteen minutes. Wave spectra are computed at each grid point, discretized into 32 frequencies and 48 directions. High directional resolution is required for a better description of wave refraction, especially in strong rotational current (Ardhuin et al., 2017; Marechal and Ardhuin, 2021). The surface current forcing fields are from de Marez et al. (2020b)'s simulations output. In one case we considered the initial shape of the cyclonic eddy (Fig. 1(a,c)). In the other case, we considered the fully developed state of the cyclonic eddy (Fig. 1(b,d)). In

145 the following, this cases are called the initial and the fully developed cases, respectively. The initial eddy case is similar to the former works performed over analytical eddy (Mathiesen, 1987; Holthuijsen and Tolman, 1991; White and Fornberg, 1998; Gallet and Young, 2014). The variation timescale of the current is much longer ($\mathcal{O}(1)$ week) than the waves (($\mathcal{O}(1)$ minute). So it respects the steady current assumption during one wave train propagation. The eddy described in previous section and in de Marez et al. (2020b) is an averaged composite eddy reconstructed from measurements in the Arabian Sea (de Marez et al.,

150 2019). The method of reconstruction tends to an underestimation of the eddy intensity, that is why the intensity of the current has been multiplied by two to increase the potential effects of currents on wave properties. The eddy is staying geophysicaly realistic (current velocity remains around 1 m.s^{-1} and normalized vorticity lower than 2, Fig.1). Those values are comparable with surface vorticity measured in the first hundred meters of Arabian sea (de Marez et al., 2020a) and in other current regimes as in the western boundary currents (Tedesco et al., 2019; Gula et al., 2015a). Although the eddy field represented in Fig.1 is

155 from an averaged composite eddy (solely estimated using in-situ data), it has been considered, in this study, as realistic because differs from an analytical vortex. Also, it has been compared with altimeter and drifter data in the region where it has been estimated. The cyclonic eddy was coherent with those measurements (see Fig.12, 13, and 14 of de Marez et al. (2019)).
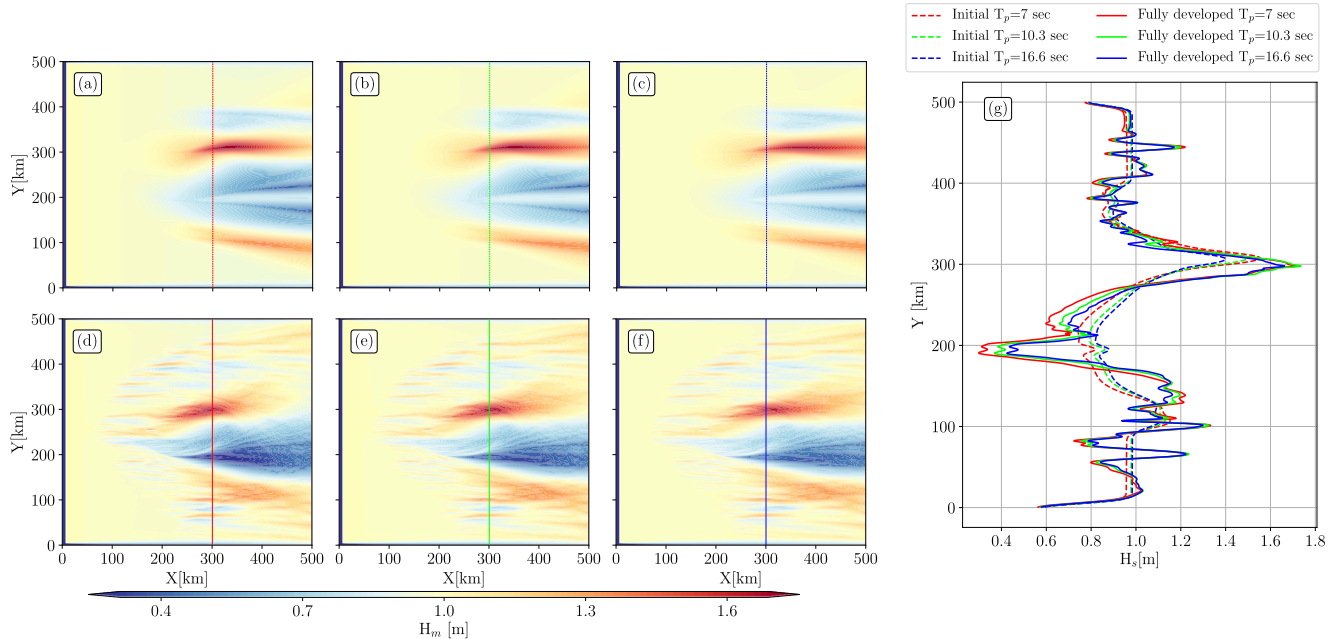
Figure 2. Significant wave height (H$_s$) fields for (a,d) T$_p$=7 s, (b,e) 10.3 s, and (c,f) 16.6 s incident waves. Without current forcing the entire domain is equal to the initial H$_s$ (1m). The first row (a,b,c) shows fields for simulations forced with the initial eddy (Fig. 1(a,c)); the second row (d,e,f) shows the same fields but for simulations forced with the fully developed eddy (Fig1(b,d)). Panel (g) shows H$_s$ along X = 300 km (colored dashed/solid lines in left panels) for all simulations.

3   Wave field variability in a cyclonic and realistic eddy

The frequency sensibility of the incident waves is studied both in the initial and in the fully developed eddy. Waves are dispersive in deep water, their group and their energy propagates at the group velocity (C_g). For T$_p$=7 s (T$_p$= $\frac{1}{f_p}$), T$_p$=10.3 s and T$_p$=16.6 s, group velocity are 11, 16, and 26 m.s^{-1}. To reach X=X$_0$ (a given value of horizontal scale) shorter waves take more time than longer waves. As waves are generated continuously from the left boundary a stationary state is reached after a sufficiently long simulation time. In Figs. 2, 3, and 4 fields are taken once the stationary state is reached. Surface currents modulate the wave amplitude, the wave frequency and the waves direction, the variability of those quantities are highlighted through H$_s$, T$_{m0,-1}$, and θ_p fields. The response of other waves variability for this underlying current, as the directional spreading or the mean direction, are not described in this manuscript.

3.1 Modulation of wave parameters

3.1.1 Significant wave height

Surface currents induce a strong regional H_s variability, specially in a highly solenoidal field (Ardhuin et al., 2017; Villas Bôas et al., 2020). Outputs of wave simulation performed in the initial and in the fully developed eddy are given in Fig. 2. The presence of an underlying vortex induce strong ∇H_s, inside and outside the eddy. Simulations forced with the initial eddy (2a,b,c) show coherent alternate sign H_s structures along meridians (fixed X−axis). An important lens shape dipole of H_s increase and decrease is noticeable in the field. H_s reaches a maximum of 1.62 m at X=333 km and Y=311 km for simulation initialized at T_p=7 sec, 1.62 m at X=349 km and Y=310 km for simulation initialized at T_p=10.3 sec, and 1.57 m X=365 km and Y=310 km for simulation initialized at T_p=16.6 sec. A transect at X=300 km is given for each initialization in Fig. 2g. Two maximums are noticeable, the main one at Y=310 km and a secondary at Y=125 km. Two minimum are noticeable, one at Y=200 km (H_s= 0.8 m) and a secondary one within Y=380 km (H_s=0.85 m). One can see that more incident waves are short more are the extremes values measured at constant X. Globally, H_s follows the current vorticity signal (Fig.1c). The enhanced H_s areas are associated to the boundary of the inner eddy core ($\zeta > 0$) and the vorticity ring ($\zeta < 0$) that surround the eddy core. Where waves are propagating against the current, H_s is enhanced which agree with waves-eddies interactions simulated in realistic fields ; (see Fig. 6 of Romero et al. (2020) and Fig.1 of Ardhuin et al. (2017)).

Simulations forced with fully developed eddy show stronger spatial inhomogeneities in the wave field (Fig. 2d,e,f). As noticed for simulations forced with the initial eddy (2a,b,c), the H_s field is matching pretty well with the cuusedrrent forcing (Fig. 1b), in other word where surface current gradients are important, strong ∇H_s are noticed. H_s is mostly modulated by the fully developed eddy core. The modulation of H_s by the eddy core occurs $\sim$ 50 km more upstream (smaller X value) than for simulations forced with initial eddy. Let us notice that ∇H_s are apparent in the submesoscale eddies that have been emerged spontaneously all around the eddy core. In the submesoscale eddy field, wave field show alternate sign of H_s variabilities, with globally the same intensity whatever the incidence frequency. It is explicitly shown in Fig. 2g at Y<180 km and Y> 350 km for each initialization. In the same transect, at Y=200 km, we can do the same remark as previously, more incident waves are short more ∇H_s are sharp. However at X=300 km and at Y corresponding to submesoscale eddies, the ∇H_s are identical whatever the initialization of waves. The H_s in the fully developed eddy are more scattered (mostly zonally due to the initial direction of the incident wave packet) than in the initial eddy. ∇H_s are sharper for simulations forced with the fully developed eddy and higher extreme values are reached. One can see that ∇H_s are important dowstream the eddy field. The horizontal size of H_s patches (intensified or decrease H_s structures) are comparable to the width of the eddy (Fig.4a-f). Finally one can see that for all simulation the signature of the eddy in the H_s field is not totally symmetric whereas the two forcing current field seemed to be so.
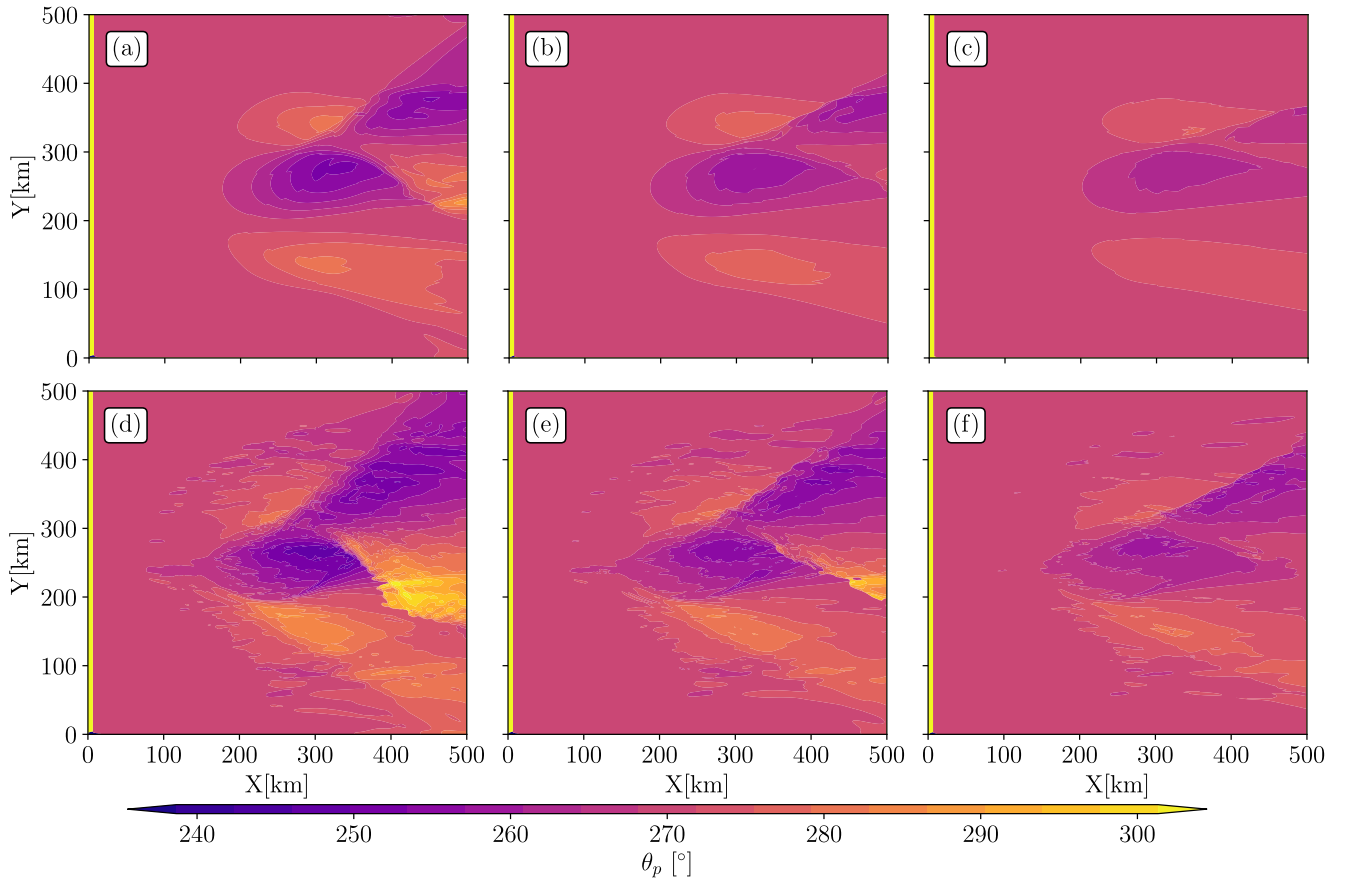
3.1.2 Peak direction

The effect of currents on wave directions can be captured to the first order by the θ_p field. Waves are turning in the current field due to refraction, globally toward the South (θ_p increase) in the bottom part of the domain and toward the North (θ_p

decreases) in the upper part. When waves pass through the eddy, θ_p changes due to the vorticity field, at X=125 km for the initial eddy (Fig.3a,b,c), and slightly upwind, at X=79 km, for the fully developed eddy (Fig.3d,e,f). Patterns showed in Fig. 3 are similar to the H_s gradient patterns showed in Fig. 2 with a large-scale dipole for simulations forced with initial eddy and both large-scales and small-scales signal gradients for simulations forced with the fully developed eddy. Narrow yellow bands in the left part of each panels are spurious, they marked the boundary where waves are generated at the left boundary. The peak direction gradient ($\nabla\theta_p$) intensity depends both on the incident wave frequency and the underlying vorticity field (Dysthe, 2001; Kenyon, 1971). $\nabla\theta_p$ is stronger for simulations initialized with T_p=7 s (Fig. 3a,d) than for simulations initialized with T_p=10.3 s and 16.6 s. In the same way, $\nabla\theta_p$ is enhanced for simulations forced with the fully developed eddy (Fig. 3d,e,f) where current field shows more smaller current features. The result corroborates Villas Bôas et al. (2020)'s findings where authors forced wave model with synthetic surface currents inverted from Kinetic Energy spectrum (with a random phase). The more turbulent the current was, the more waves were refracted. Refraction can induce a change of θ_p that can reach $\pm 30°$ for simulation initialized by T_p=7 sec and forced with the fully developed eddy (Fig.3d). Very long waves trains (T_p=16.6 sec) hardly reach a deviation of wave direction higher than $10°$, both in fully developed and initial eddy. Finally one can see that θ_p differs downstream the eddy with respect to the initial direction ($270°$), waves keep in memory the effects of surface currents

3.1.3 Mean wave period

As surface currents have an effect on the wave frequency (Phillips, 1977) due to the conservation of the absolute frequency, Eq.(2), surface currents modified $T_{m0,-1}$. Wave simulations are initialized with different wave peak frequencies, so directly impacting the values of $T_{m0,-1}$. The different initializations of the wave field justify the representation of the relative difference of $T_{m0,-1}$ ($\Delta T_{m0,-1}$) rather than raw outputs. This $\Delta T_{m0,-1}$ is the difference between outputs of simulations performed with and without surface current forcing (Fig.4). At first glance, the spatial inhomogeneities are more striking for simulations forced with the fully developed eddy, similar to the H_s and θ_p fields (Fig. 2, 3). For a fully developed eddy, $\Delta T_{m0,-1}$ exceeds 3 sec in the eddy core for X between 200 km and 400 km. For initial eddy forcing $\Delta T_{m0,-1}$ does not goes above 2 sec at the same location (Fig 4g). As for H_s field, the $\Delta T_{m0,-1}$ does not much depend on the frequency of the incident waves, or at least, not as much as $_theta_p$ field studied above. Slight differences are however noticeable for simulations forced with fully developed eddy. This is not clear if there is a link between the incident wave frequency and the slight differences in $\Delta T_{m0,-1}$ signal especially in the submesoscale eddies where $\Delta T_{m0,-1}$ are stronger for long incident waves whereas we see the opposite in the core of the fully developed eddy. $\Delta T_{m0,-1}$ are positive where waves and current are propagating in the same direction and vice versa. This change of $\Delta T_{m0,-1}$ is because current induce a Doppler shift on the wave frequency (Eq.(2)) and that the absolute frequency is conserved. Where waves and current are opposite we see that H_s are enhanced (Fig.2) and waves wavelength are shortened. It is due to the conservation of wave action ($D_t N = 0$, Eq. (1)) If we focus on the maximum of $\Delta T_{m0,-1}$ at Y=200 km, waves are extended of about 153 m and H_s decreased of about 0.65 cm. One can see that waves stripes induced by refraction (Fig. 3) are also captured in the mean wave period signal and that waves are shorter (smaller $T_{m0,-1}$) where H_s were enhanced (Fig. 2). We precise that the change of H_s induced by current is due to a superposition of processes. Indeed, in current field, in the absence of wind, regional H_s variability results from the wave refraction and the advection of

Figure 3. Peak direction (θ_p) field for (a,d) T_p=7 s, (b,e) 10.3 s, and (c,f) 16.6 s incident waves. Without current forcing the entire domain is equal to the initial θ_p (270°). The first row (a,b,c) shows fields for simulations forced with the initial eddy (Fig. 1(a,c)); the second row (d,e,f) shows the same fields but for simulations forced with the fully developed eddy (Fig. 1(b,d)).)

waves action by the current and the group speed (Ardhuin et al., 2017). The doppler-shifted wave frequency by current can also increase the H_s (see introduction of Benetazzo et al. (2013)). Note that current refracts waves such that waves and current can becomes aligned (or opposite). So refraction can trigger a change of mean wave period downstream the refraction areas in the same manner that refraction induce a non-local change of H_s.

For all the variable studied here (Fig.2,3, 4), waves are continuously generated at the left boundary, a solitary incident wave train affect strongly the results presented above, for instance the non-local effect of refraction on the wave field is strongly less pronounced (not shown).
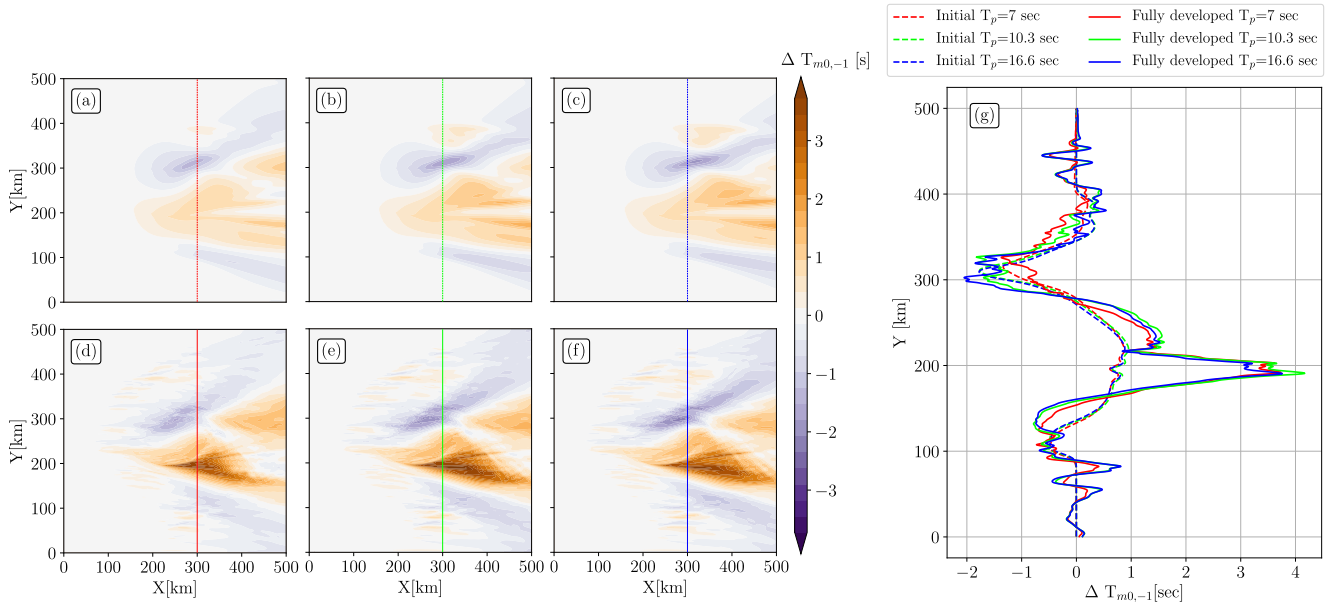
Figure 4. Mean wave period difference ($\Delta T_{m0,-1}$) between simulations forced with and without current ($\Delta T_{m0,-1} = T_{m0,-1}$(curr)-$T_{m0,-1}$(Nocurr)). Panels (a,d) show $\Delta T_{m0,-1}$ fields initialized by T_p=7 s wave group. Panels (b,e) show $\Delta T_{m0,-1}$ fields initialized by T_p=10.3 s. Panels (c,f) show $\Delta T_{m0,-1}$ fields initialized by T_p=16.6 s. The first row (a,b,c) shows instantaneous fields for simulations forced with the initial eddy (Fig.1(a,c)); the second row (d,e,f) shows the same fields but for simulations forced with the fully developed eddy (Fig.1(b,d)). Panel (g) shows $\Delta T_{m0,-1}$ along X = 300 km (colored dashed/solid lines in left panels) for all simulations.

3.2 Ray tracing

In a rotational current field, wave rays are bent because of refraction. The wave energy spectrum ($E(\sigma, \theta)$) is not conserved in surface currents. Indeed waves and currents exchange energy. Nevertheless wave action ($N(\sigma, \theta)$) is conserved (Bretherton and Garrett, 1968). In a strong rotational current field, the change of H_s is mostly driven by refraction from mesoscale and submesoscale current (Irvine and Tilley, 1988; Ardhuin et al., 2017; Romero et al., 2020). In the present study, the isolated vortex modifies waves which results in a strong H_s and $T_{m0,-1}$ field inhomogeneity (Fig. 2, 4). This current-induced refraction is highlighted here thanks to a Monte-Carlo ray tracing simulation. The ray-tracing assumes that surface currents are stationary ($\frac{|u|}{C_g} \ll 1$) and that incident waves are monochromatic. In a real ocean, wave field is a superposition of wave trains with specific directions and frequencies, thus ray tracing is only a very simplified view of how the direction of the waves are modified by the presence of current. Thanks to the ray equation (Eq.3), we expect that refraction is more important where waves and currents vectors are perpendicular (see the $\dot{\theta}$ in Eq.(2) of Ardhuin et al. (2017) or Eq.(17) of Villas Bôas et al. (2020).) Examples of ray-tracing are shown in Fig. 5 in both the initial and fully developed eddy.

The initialized direction is 270° (waves are coming from the left boundary) and the initial frequencies are the same than the ones discussed above (T_p =7 s, 10.3 s, and 16.6 s peak periods). We see that the refraction induced by the surface currents

11

is sensitive to both the nature of underlying current and the frequency (or wavelength) of the incident waves. The radius of curvature of waves rays is larger where the current field is highly rotational (Fig. 5d,e,f) and when simulations are initialized with T_p=7 s waves (Fig. 5a,d) (Kenyon, 1971; Dysthe, 2001). In the initial eddy case, the wave train is refracted both by the eddy's edge (toward the South) and the core of the eddy (toward the North) (Fig. 5a,b,c). It leads to two wave rays focalisation areas downstream the initial eddy. These focalisation areas, or caustics, are slightly shifted zonally toward the right boundary when the incident wave are longer. The caustic in the upper part of Fig.5 (a,b,c) appears at X=330 km, X=370 km, and X=445 km respectively. In the fully developed field, both mesoscale and submesoscale features refract waves. One can see that the number of caustics increases in the fully developed eddy with a maximum of caustics for T_p= 7 s incident waves (Fig. 5d). Even if isolated submesoscale eddies have a vorticity comparable with the eddy core ($\frac{\zeta}{f_0} \sim 1.5$), they do not refract waves as much as the center structure does. Indeed, if we look at the southernmost submesoscale eddy we see that one wave-ray is deviated of about 30 km from the left boundary to the right boundary whereas one wave ray at the center of the domain is deviated of more than 200 km. The frontal dynamic at the boundary of the main structure of the fully developed eddy induce the strongest wave-ray deviation whereas there scale and their relative vorticity is comparable to submesoscale eddies structures. So the shape of vorticity patterns is key in the intensity of the refraction. One can notice that rays convergent areas are localised where H_s reaches peaks (Fig. 2), specially at the edge of the positive vorticity core. Through realistic numerical studies in strong current fields, Ardhuin et al. (2012) and Kudryavtsev et al. (2017) showed qualitatively the link between rays caustics and realistic H_s enhancement.

The strong vorticity field both for initial and fully developed cyclonic eddy induces a wave rays scattering which can reach a deviation of several hundred kilometers with respect to a propagation without background current. This deviation is more important for short waves incidence (Fig. 5a,d). The strong wave-scattering can be responsible of the space-time bias in the forecast of waves arrival (Gallet and Young, 2014; Smit and Janssen, 2019). The ray tracing study shows that refraction have a local effect on wave direction, strong ray deviations appear where ∇U are strong. However, refraction effects on wave parameters are non-local. We saw that H_s enhancement and wave ray caustics can appear both inside and outside the eddy (Fig.2,5). In other word, strong ∇H_s are not necessarily at strong ∇U locations.

4 Is it possible to reconstruct ∇U *via* the measurement of the ∇H_s?

The ∇H_s at scale between 200 km and $\sim$10 km are associated to the nature of the underlying current (structure and intensity). The current intensity gradients ∇U ($\sqrt{\partial_x U^2 + \partial_y U^2}$) and more specifically the vorticity of the flow, induces refraction resulting in ∇H_s patterns correlated to vorticity patterns (Villas Bôas et al., 2020). Note that both ∇U and ∇H_s are scalars. Assuming that the group speed of waves are much bigger than the intensity of the current velocity,

$$\frac{U}{C_g} << 1, \tag{6}$$

and that waves are stationary, the conservation of wave action simplifies to,

$$\frac{H_s}{\sigma} = Cte, \tag{7}$$
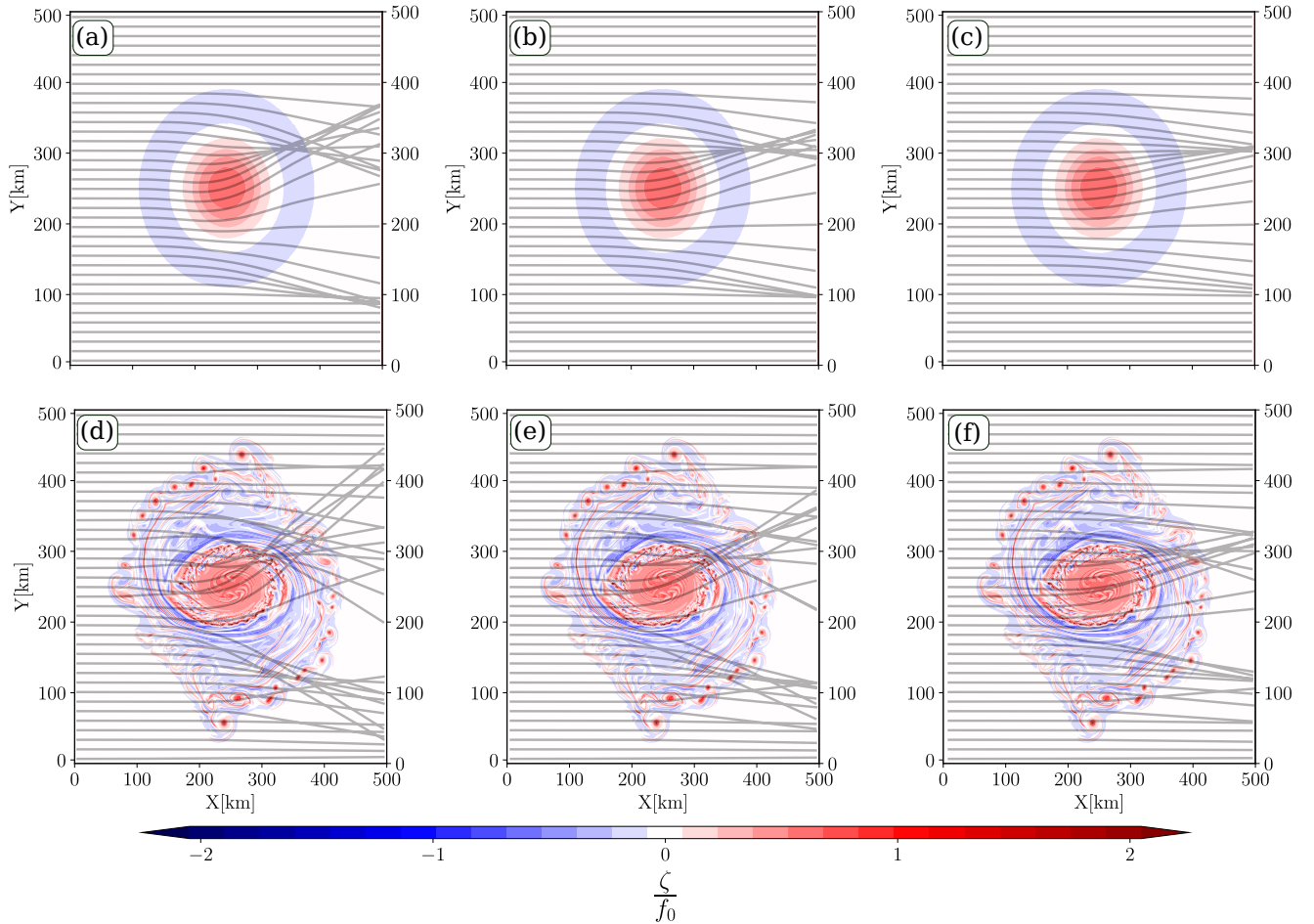
Figure 5. (a,b,c) Ray tracing for waves travelling over the initial eddy with $T_p = 7$ s, (a) 10.3 s (b), and 16.6 s (c) peak period. (d,e,f) same but for waves travelling over the fully developed eddy. The vorticity fields are given in the background.

leading to the first order approximation:

$$\frac{\nabla H_s \sigma}{(H_s k)} \sim \nabla U. \tag{8}$$

The Eq.(8) shows that ∇H_s is function of surface current gradients, wave steepness ($k H_s$) and wave incident frequency. Steps to retrieved the Eq.8 are given in Appendix 1. The motivation of this paragraph is to know if, from high-resolution-wave measurements from filtered altimeter data (Dodet et al., 2020), spectrometers (Hauser et al., 2020) or from optic images (Kudryavtsev et al., 2017), the nature of the flow can be estimated. Today's surface currents measurements from Sea-Level-Anomaly can capture eddy with a shape similar to Fig.1a,c (if their lifetime are sufficiently long according to the revisiting-time of altimeters). However eddy with a more realistic shape (Fig.1b,d) are very poorly captured (see section 5.2 of de Marez et al.

13
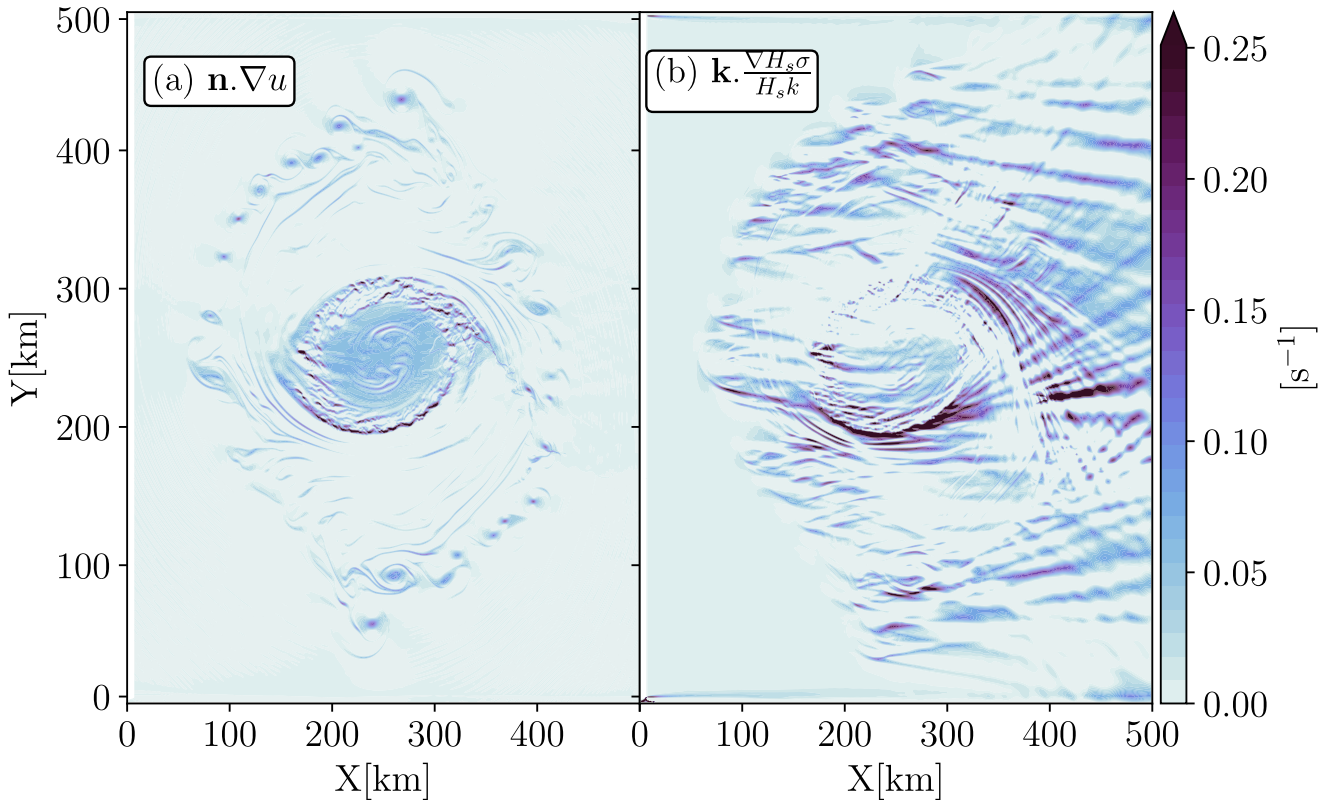
Figure 6. (a) Surface current gradients (∇u) projected perpendicular to the peak wave direction vector, *i.e.* the right hand side of Eq. (8) and (b) normalized wave height gradient ($\frac{\nabla H_s \sigma}{H_s k}$) projected in the peak wave direction vector, *i.e.* the left hand side of Eq. (8), both for the fully developed eddy. These instantaneous fields are for simulation initialized with $T_p = 7$ s.

(2020b)). Thanks to our numerical results we will test the validity of Eq.8 in the case of fully developed eddy. The final aim is to know if the nature of the flow can be estimated by inverting high resolution H_s, σ (or k) measurements. Right and left hand sides of Eq. (8) are shown in Fig. 6 (a,b) in the fully developed eddy case, for incident waves at $T_p=7$ s. ∇H_s and ∇U have been projected along and perpendicular to the wave peak direction respectively. Both terms of Eq. (8) are of the same order of magnitude with values slightly higher for the $\frac{\nabla H_s \sigma}{(k H_s)}$ field (Fig. 6b). ∇U shows rounded structures (Fig. 6a) whereas ∇H_s field shows more elongated-horizontal structures aligned with the initial wave direction (270°). From X=0 km to X=250 km, normalized ∇H_s patterns are aligned with the incident wave directions, downstream X=250 km patterns follow the rays trajectories shown in Fig.5d. Apart from the difference of shape, both fields are matching both at mesoscale (the central eddy) and at smaller scale (submesoscale eddies around the core of the ellipsoidal eddy) from X=0 km to X=250 km. ∇U exhibits fronts at the boundary of the central eddy also captured by the normalized ∇H_s field. Inside the central ellipsoidal eddy (between Y=200 km and 300 km), ∇U shows a smooth and homogeneous field which is captured in Fig. 6b

14
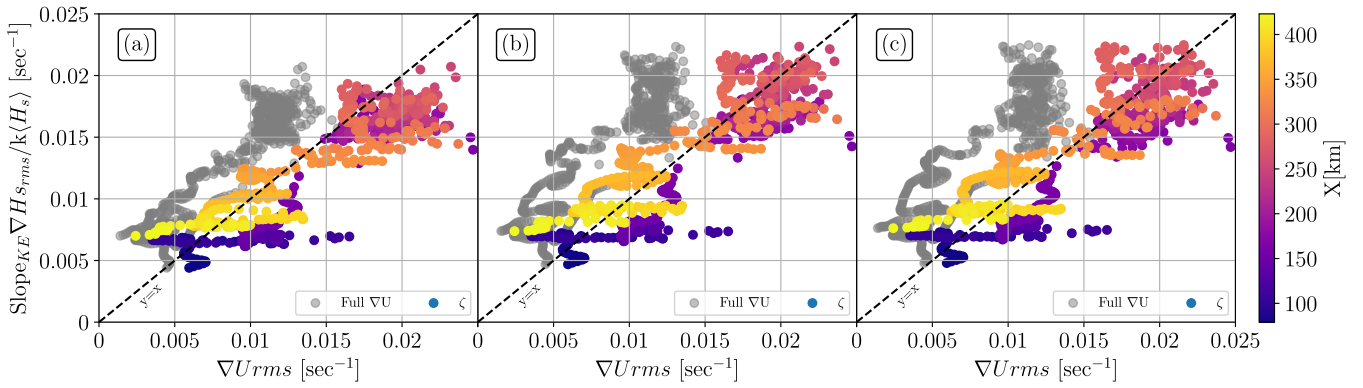
Figure 7. Scatter plot of the normalized root-mean-square of significant wave height gradients as a function of root-mean-square surface current gradients. Colored points are the scatter plot for the vorticity component of the surface current gradients and grey points for the full surface current gradient (diverging component + rotational component). One point correspond to the root-mean-square of the two quantities for constant X, the value of X is given as colorscale. $<H_s>$ is the average value of the significant wave height when simulations reach the stationnary state. Panel (a), (b) and (c) are for simulations forced with the fully developed eddy initialized with T_p=7 sec, T_p=10.3 sec, and T_p=16.6 sec respectively.

only between Y=200 km and 250 km. Reader can also see discrepancies between the two fields, between the central eddy and the submesoscales eddies, where sharp ∇H_s are shown whereas ∇U are very smooth. Downstream the eddy even if ∇U is null (Fig.6a), normalized ∇H_s are very sharp (Fig.6b). The non-local effect of current gradients on the H_s is thus well highlighted through this diagnostic.

310   The analysis of Fig. 6b shows that the wave simulations capture surface currents gradient in the first half of the domain, without any information on surface current. The inversion of the ∇H_s to infer the underlying surface currents seemed to be promising, however both the non-local effect of currents on waves and the initial incidence direction (resulting in a privileged direction of ∇H_s patterns) show that the phase of current gradient is hardly reproduced in most of the part of the domain. It proved some limitations in the ∇H_s inversion to infer ∇U. To better describe the robustness of the formula given in Eq. 8

315 we proposed a scatter plot of the root-mean-square (rms) of the left hand side as a function of the rms of the right hand side of Eq.(8). Results are given in Fig.7. As proved numerically by Villas Bôas et al. (2020), we have multiplied the left-hand-side of Eq.(8 by 3 which is the absolute value of the slope of the Kinertic Energy spectrum of the fully developed eddy. A point in Fig.7 is the rms of the normalized ∇H_s and of the ∇U at fixed distance from the left boundary. The diagnostics have been done both for the full gradients of the surface currents (divergence and vorticity) and only for the vorticity component. Villas Bôas

320 et al. (2020) proved that ∇H_s is strongly proportional to the vorticity component of the flow (see their Fig.12), we wanted to show here the effect of the divergence on the proportionality between ∇H_s and ∇U. The divergence component of the surface gradients is one order of magnitude smaller than the rotationnal one (not shown.) We do not focus on the gradients for X<79 km and X>423 km because ∇U are null. Thanks to a linear regression between points in Fig.7, we verified that ∇H_s and ∇U (vorticity) are strongly proportional. Slope are equal to 1.13 (0.72), 1.20 (0.8), and 1.17 (0.8) for simulations initialized with

15

325 T_p=7 sec, T_p=10.3 sec, and T_p=16.6 sec. However the coefficient of determination (R2) is negative for the rms of the full ∇U with respect to ∇H_s meaning that the linear relation between ∇H_s and ∇U is not verified. When the rms of ∇H_s is compare to the rms of ζ we confirm the results of Villas Bôas et al. (2020) between X=79 km and X=423 km with R2 varying within 0.67 and 0.75 for all initializations.

Where oceanic eddy becomes unstable spontaneously due to horizontal sheared current structures (barotropic instabilities)
330 or vertical buoyancy gradient (baroclinic instabilities, mixed layer instabilities), the resulting ocean surface shows specific ∇U features. Thanks to wave numerical experiments we were able to observe ∇H_s structures which are similar to the structures of ∇U and more specially to the vorticity component of ∇U. The amplitude of the two gradients are comparable if we know the nature of the incident waves. It seems promising to invert the waves signal to infer the underlying vorticity field and, perhaps, the instabilities that created such structures (according to the shape and the size of ∇H_s). Optical instruments have shown
335 there robustness to retrieve both the phase and the amplitude of the waves field at an unprecedented spatial resolution (~ 10 m) in a very wide swath (Kudryavtsev et al., 2017)). The use of such instrument seems to be a good candidate to capture very small-scale current features by inverting wave characteristics as shown in the fully developed eddy. Nevertheless there is one drawback, and not least, the non-local effects of current on H_s which make emerge ∇H_s where current is null.

Measuring surface currents from space is a very challenging purpose since past decades (Villas Bôas et al., 2019). Al-
340 timetry has proved its robustness to capture surface geostrophic current at global scale by measuring the along track Sea-Level-Anomaly from multiple altimeter missions. The effective resolution of the current depends principally on the number of satellites. The resolution of global map of surface currents derived from altimetry has been calculated and show a mean effective resolution higher than 250 km at mid-latitudes and more than 600 km in the equatorial band (Rio et al., 2014; Ballarotta et al., 2019). Even if mesoscale eddies are observable from space (Chelton et al., 2011), surface dynamics at smaller scales
345 are not captured by present altimeter products. As an example we can cite the small oceanic features in the fully developed eddy (see section 5.2 section of de Marez et al. (2020b)). This reality has highlighted the necessity to measure surface currents at higher resolution triggering the emergence of new satellite missions based on innovative measurements methods (Ardhuin et al., 2018; Morrow et al., 2019; Ardhuin et al., 2021).

5 Effects on broader banded incident spectra and nonlinear wave-wave interactions on wave-current interactions

350 ### 5.1 New model setup

In the previous analysis the incident waves have been simulated via wave spectra gaussian in frequency with a frequency spreading (σ_f) equal to 0.03 Hz. For time scale much larger than the wave period and a gaussian surface, nonlinear wave-wave interaction trigger a change of the wave energy in the wave field Hasselmann (1962). Here we wanted to quantify the effects of nonlinear wave-wave interactions on the wave parameter gradients in a current field. To study the cross-spectral energy flux
355 between frequencies we activated the nonlinear source term (S_{nl}). The right hand side of Eq.(1) was thus not equal to 0 any more but to S_{nl}. Because simulations initialized with very narrow banded spectrum do not show a clear difference between simulations with and without S_{nl} (not shown), we extended the frequency spreading of the incident wave trains to σ_f=0.1

Hz. For sufficiently steep waves, nonlinear wave-wave interactions redistribute wave energy between frequencies over the spectrum which strongly modifies the shape of the spectrum (Komen et al., 1984). As ∇H_s is function of the wave steepness (kH$_s$, Fig.8) we expected that nonlinear wave-wave interactions would have an impact on the intensity of the wave parameters gradients. Nonlinear wave-wave interactions have been modeled using the discrete interaction approximation (Hasselmann et al., 1985). The wave simulation has been run during a sufficiently long time to capture the long term effect of nonlinear wave-wave interactions on the wave parameters. Wave simulation has been performed only for 7 sec incident waves over the fully developed eddy field. This section is a simple introduction of how both wave-wave interactions and wave-current interactions could induced inhomogeneity in the wave field still in a very idealized framework. Further investigation wil be required.

5.2 Results

For a given wave parameter (H$_s$ or T$_{m0,-1}$), the relative difference has been computed between simulations where nonlinear source term was activated and desactivated (Eq.9),

$$\Delta X = \frac{X_{S_{nl}} - X_{noS_{nl}}}{X_{noS_{nl}}} \times 100. \tag{9}$$

The nonlinear wave-wave interactions have a large effect on the spatial gradient of wave parameters studied before, H$_s$ are globally enhanced whereas T$_{m0,-1}$ are decreased (Fig.8). The spatial variability of the H$_s$ can reach +80% for X>250 km at Y$\sim$200 km when S$_{nl}$ is activated. It has been shown that at the same location, wave-current interactions alone showed a strong decrease of H$_s$ (Fig.2). One can see also that simulation with wave-wave interactions enhance the H$_s$ at the periphery of the eddy core of the fully developed eddy, in the submesoscale eddy field area. Globally, we see that H$_s$ increases where wave-currents interactions have decrease the H$_s$. One can see that areas where enhancement of H$_s$ have been noticed in Fig.2 are not modified in Fig.8a or only slightly. Please notice that we cannot compare quantitatively Fig.8a and Fig.2d because the incident waves have a different spreading in frequency. Nonlinear wave-wave interactions also highlight a change in the T$_{m0,-1}$ field. ΔT$_{m0,-1}$ shows the opposite spatial variation of Δ H$_s$. Indeed, where Δ H$_s$ were (strongly) positive, ΔT$_{m0,-1}$ is (strongly) negative and vice versa. A transects at X=300 km show the values of H$_s$ and T$_{m0,-1}$ along the vertical (Fig.8c,d). One can see that ∇ H$_s$ are globally reduced due to nonlinear wave-wave interaction specially in the core of the central eddy (Y between 200 km and 350 km). At location of submesoscale eddies, ∇H_s are also sharper for simulation without S$_{nl}$ but the difference between the two parametrizations are less pronounced. ∇ T$_{m0,-1}$ show a much more striking difference between simulations with and without nonlinear wave-wave interactions,. ∇ T$_{m0,-1}$ are the most pronounced also in the core of the eddy where wave period can reach a 4 sec difference whereas simulation with S$_{nl}$ reveal only a change of 2 sec. Whether for H$_s$ or T$_{m0,-1}$, in current field, wave-wave interactions have the tendency to decrease spatial gradients of the wave parameters triggered by wave-current interactions. Here the choice of the parametrization of the nonlinear wave-wave interactions was arbitrary (Hasselmann et al., 1985), it would be interesting to expand this study to other parametrizations of S$_{nl}$ to better describe how nonlinear wave-wave processes modify regional wave parameter gradients.

17
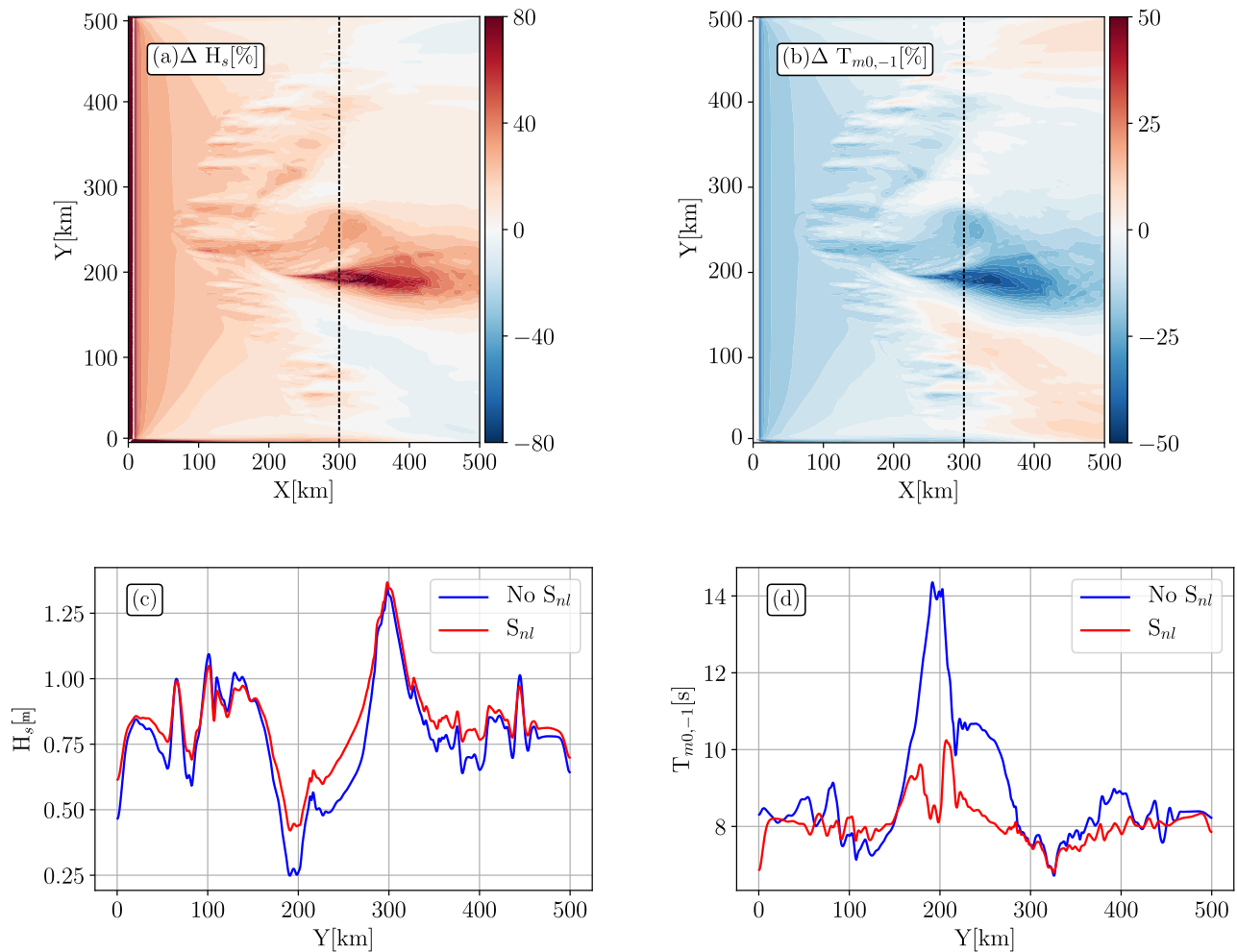
Figure 8. Model difference between solutions with and without nonlinear wave-wave interactions. Panel (a) and (b) show the relative difference in percent of the significant wave height and the mean wave period. Panel (c) and (d) show a transect at X=300 km for simulations without (solid blue line) and with (solid red line) nonlinear source term (S_{nl}) for H_s and $T_{m0,-1}$ respectively

6 Conclusion and perspectives

In this paper, we studied numerically the effect of an isolated composite cyclonic eddy on the wave properties. High resolution wave simulations have been forced by a composite eddy reconstructed from in-situ measurements in the Arabian Sea. The wave model has been forced on the one hand by the initial eddy field (gaussian shape) and, on the other hand, by the fully developed eddy resulting from the destabilization within the composite eddy. Waves have been simulated by the use of a third generation phase averaged spectral model initialized with narrow wave spectra centered at different frequencies (T$_p$ =7 , 10.3, and 16.6 s). Although wave scattering by an oceanic vortex has already been studied in former papers (Mapp et al., 1985; White and Fornberg, 1998; Gallet and Young, 2014), this study completes studies performed in the past with *(1)* a description of the evolution of the wave bulk parameters as significant wave height and mean wave period inside and outside the isolated vortex, and *(2)* the investigation of how a fully developed eddy (that really occur in a real ocean) modify the wave field. Both wave dynamic and kinematics are changed by the presence of an underlying current. These changes are more pronounced where the underlying current gradients are strong and when incident waves are short. This is coherent with the studies of Kenyon (1971); Dysthe (2001). As multi-scale dynamic eddies are certainly more realistic in the ocean than gaussian eddies, former studies of interaction between wave and gaussian eddy underestimate wave refraction, extreme significant wave heights but also wave steepness because surface currents also induce a non negligible change of wave period (wavelength). Those underestimations can have a large impact on the waves forecast but also on the source of noise induced by waves in the ocean level measurements by altimeters. Tran et al. (2010) proposed to combined altimeter measurements and wave simulations in order to develop a global sea-state bias model. Thanks to the period provided by wave model (only forced by wind) authors showed the possibility to reduce the error budget of ∼7.5%. However they parametrized their wave model on a too much coarse grid (1° × 1°) without taken into account current forcing. As we proved here, short-scale currents induce large changes of wave period at regional scale (smaller than wind scale patterns). Indeed, even in a very idealized eddy, $\Delta T_{m0,-1}$ oscillates within 1 sec (Fig. 4a-c) and reaches ∼3 sec for a more realistic eddy pattern (Fig. 4a-c). Redo the same work of Tran et al. (2010) at higher resolution with current sufficiently resolved (Marechal and Ardhuin, 2021) would be benefit to improved their sea-states bias model at regional scale.

Under the WKB approximation and in the geometric theory framework, the significant wave height gradients normalized by the incident wave frequency has been described as a function of the surface current gradients. Besides a good coherence in terms of magnitude between the two quantities, structures of significant wave height gradient are very sensitive to the underlying surface current. We know that measurements of sea level anomaly from space are able to monitoring surface currents at global scale with a wavelength resolution of several hundreds kilometers in a ice-free areas (Villas Bôas et al., 2019). All the surface dynamics at smaller scales cannot be captured by altimeters whereas a lot of oceanic processes occur at those scales (from 1-100 km). This manuscript have shown the possibility to infer the vorticity of the eddy field from the inhomogeneity in the waves field, as proposed in Villas Bôas et al. (2020). Infer vorticity patterns could allow to capture the small-scale processes (vertical movements, mixing, shear flows...) without measurement of surface currents. Nevertheless, this inversion could not works in the vicinity of a strong ∇U field because waves keep in memory the effect of upstream currents resulting in a regional

inhomogeneity in the wave field even if the current gradients are null. As measuring surface currents both at global scale

425   and high resolution being a present challenge for the oceanographic community, different strategy have been imagined. Infer ∇U from ∇H_s seemed to be a good strategy, but because the wave-current coupled system is too much complex, much more than the one proposed here, assumption proposed in this manuscript are hardly satisfied in nature. Moreover, even in a very simplified framework as proposed here, the wave inversion is, at the best, only partial. So one possible solution would be a direct measurement of surface currents from space as proposed in Ardhuin et al. (2018).

430   *Data availability.* The cyclonic vortex field is available at https://data.mendeley.com/datasets/bwkctkk5bn/1.

References

Ardhuin, F., Roland, A., Dumas, F., Bennis, A.-C., Sentchev, A., Forget, P., Wolf, J., Girard, F., Osuna, P., and Benoit, M.: Numerical wave modeling in conditions with strong currents: Dissipation, refraction, and relative wind, Journal of Physical Oceanography, 42, 2101–2120, 2012.

435 Ardhuin, F., Rascle, N., Chapron, B., Gula, J., Molemaker, J., Gille, S. T., Menemenlis, D., and Rocha, C.: Small scale currents have large effects on wind wave heights, J. Geophys. Res., 122, 4500–4517, https://doi.org/10.1002/2016JC012413, 2017.

Ardhuin, F., Aksenov, Y., Benetazzo, A., Bertino, L., Brandt, P., Caubet, E., Chapron, B., Collard, F., Cravatte, S., Dias, F., Dibarboure, G., Gaultier, L., Johannessen, J., Korosov, A., Manucharyan, G., Menemenlis, D., Menendez, M., Monnier, G., Mouche, A., Nouguier, F., Nurser, G., Rampal, P., Reniers, A., Rodriguez, E., Stopa, J., Tison, C., Tissier, M., Ubelmann, C., van Sebille, E., Vialard, J., and Xie, J.:

440 Measuring currents, ice drift, and waves from space: the Sea Surface KInematics Multiscale monitoring (SKIM) concept, Ocean Sci., 14, 337–354, https://doi.org/10.5194/os-2017-65, 2018.

Ardhuin, F., Alday Gonzalez, M. F., and Yurovskaya, M.: Total Surface Current Vector and Shear from a Sequence of Satellite images: Effect of Waves in Opposite Directions, Earth and Space Science Open Archive, 2021.

Ballarotta, M., Ubelmann, C., Pujol, M.-I., Taburet, G., Fournier, F., Legeais, J.-F., Faugere, Y., Delepoulle, A., Chelton, D., Dibarboure, G., and Picot, N.: On the resolutions of ocean altimetry maps, Ocean Science Discussions, https://doi.org/10.5194/os-2018-156, 2019.

445

Benetazzo, A., Carniel, S., Sclavo, M., and Bergamasco, A.: Wave–current interaction: Effect on the wave field in a semi-enclosed basin, Ocean Modelling, 70, 152–165, 2013.

Bretherton, F. P. and Garrett, C. J. R.: Wavetrains in inhomogeneous moving media, Proceedings of the Royal Society of London. Series A. Mathematical and Physical Sciences, 302, 529–554, 1968.

450 Bruch, W., Piazzola, J., Branger, H., van Eijk, A. M., Luneau, C., Bourras, D., and Tedeschi, G.: Sea-Spray-Generation Dependence on Wind and Wave Combinations: A Laboratory Study, Boundary-Layer Meteorology, pp. 1–29, 2021.

Cavaleri, L., Fox-Kemper, B., and Hemer, M.: Wind Waves in the Coupled Climate System, Bull. Amer. Meteorol. Soc., 78, 1651–1661, 2012.

Chelton, D. B., deSzoeke, R. A., Schlax, M. G., El Naggar, K., and Siwertz, N.: Geographical Variability of the First

455 Baroclinic Rossby Radius of Deformation, Journal of Physical Oceanography, 28, 433–460, https://doi.org/10.1175/1520-0485(1998)028<0433:GVOTFB>2.0.CO;2, 1998.

Chelton, D. B., Schlax, M. G., Samelson, R. M., and de Szoeke, R. A.: Global observations of large oceanic eddies, Geophysical Research Letters, 34, https://doi.org/10.1029/2007GL030812, 2007.

Chelton, D. B., Schlax, M. G., and Samelson, R. M.: Global observations of nonlinear mesoscale eddies, Progress in Oceanography, 91,

460 167–216, https://doi.org/10.1016/j.pocean.2011.01.002, 2011.

de Marez, C., L'Hégaret, P., Morvan, M., and Carton, X.: On the 3D structure of eddies in the Arabian Sea, Deep Sea Research Part I: Oceanographic Research Papers, 150, 103 057, https://doi.org/10.1016/j.dsr.2019.06.003, 2019.

de Marez, C., Carton, X., Corréard, S., L'Hégaret, P., and Morvan, M.: Observations of a deep submesoscale cyclonic vortex in the Arabian Sea, Geophysical Research Letters, 47, e2020GL087 881, 2020a.

465 de Marez, C., Meunier, T., Morvan, M., L'Hégaret, P., and Carton, X.: Study of the stability of a large realistic cyclonic eddy, Ocean Modelling, 146, 101 540, https://doi.org/10.1016/j.ocemod.2019.101540, 2020b.

Dodet, G., Piolle, J.-F., Quilfen, Y., Abdalla, S., Accensi, M., Ardhuin, F., Ash, E., Bidlot, J.-R., Gommenginger, C., Marechal, G., Passaro, M., Quartly, G., Stopa, J., Timmermans, B., Young, I., Cipollini, P., and Donlon, C.: The Sea State CCI dataset v1: towards a sea state climate data record based on satellite observations, Earth System Sci. Data, 12, 1929–1951, https://doi.org/10.5194/essd-12-1929-2020, 2020.

Dysthe, K. B.: Refraction of gravity waves by weak current gradients, J. Fluid Mech., 442, 157–159, 2001.

Gallet, B. and Young, W. R.: Refraction of swell by surface currents, J. Mar. Res., 72, 105–126, https://doi.org/10.1357/002224014813758959, 2014.

Gula, J., Molemaker, M., and McWilliams, J.: Topographic vorticity generation, submesoscale instability and vortex street formation in the Gulf Stream, Geophysical Research Letters, 42, 4054–4062, 2015a.

Gula, J., Molemaker, M. J., and Mcwilliams, J. C.: Gulf Stream Dynamics along the Southeastern U.S. Seaboard, J. Phys. Oceanogr., 45, 690–715, 2015b.

Hasselmann, K.: On the non-linear energy transfer in a gravity-wave spectrum Part 1. General theory, Journal of Fluid Mechanics, 12, 481–500, 1962.

Hasselmann, S., Hasselmann, K., Allender, J., and Barnett, T.: Computations and parameterizations of the nonlinear energy transfer in a gravity-wave specturm. Part II: Parameterizations of the nonlinear energy transfer for application in wave models, Journal of Physical Oceanography, 15, 1378–1391, 1985.

Hauser, D., Tourain, C., Hermozo, L., Alraddawi, D., Aouf, L., Chapron, B., Dalphinet, A., Delaye, L., Dalila, M., Dormy, E., et al.: New observations from the SWIM radar on-board CFOSAT: Instrument validation and ocean wave measurement assessment, IEEE Transactions on Geoscience and Remote Sensing, 59, 5–26, 2020.

Holthuijsen, L. and Tolman, H.: Effects of the Gulf Stream on ocean waves, Journal of Geophysical Research: Oceans, 96, 12 755–12 771, 1991.

Hua, B. L., Ménesguen, C., Le Gentil, S., Schopp, R., Marsset, B., and Aiki, H.: Layering and turbulence surrounding an anticyclonic oceanic vortex: In situ observations and quasi-geostrophic numerical simulations, Journal of Fluid Mechanics, 731, 418–442, 2013.

Huang, N. E., Chen, D. T., Tung, C.-C., and Smith, J. R.: Interactions between steady won-uniform currents and gravity waves with applications for current measurements, Journal of Physical Oceanography, 2, 420–431, 1972.

Irvine, D. E. and Tilley, D. G.: Ocean wave directional spectra and wave-current interaction in the Agulhas from the shuttle imaging radar-B synthetic aperture radar, J. Geophys. Res., 93, 15 389–15 401, 1988.

Kenyon, K. E.: Wave refraction in Ocean Current, Deep-Sea Res., 18, 1971.

Kirby, J. T. and Chen, T.-M.: Surface waves on vertically sheared flows: approximate dispersion relations, Journal of Geophysical Research: Oceans, 94, 1013–1027, 1989.

Komen, G., Hasselmann, S., and Hasselmann, K.: On the existence of a fully developed wind-sea spectrum, Journal of physical oceanography, 14, 1271–1285, 1984.

Kudryavtsev, V., Yurovskaya, M., Chapron, B., Collard, F., and Donlon, C.: Sun glitter Imagery of Surface Waves. Part 2: Waves Transformation on Ocean Currents, J. Geophys. Res., 122, https://doi.org/10.1002/2016JC012426, 2017.

Le Vu, B., Stegner, A., and Arsouze, T.: Angular Momentum Eddy Detection and Tracking Algorithm (AMEDA) and Its Application to Coastal Eddy Formation, Journal of Atmospheric and Oceanic Technology, 35, 739–762, https://doi.org/10.1175/JTECH-D-17-0010.1, 2018.

Lévy, M., Franks, P. J. S., and Smith, K. S.: The role of submesoscale currents in structuring marine ecosystems, Nature Communications, 9, 4758, https://doi.org/10.1038/s41467-018-07059-3, 2018.

Mapp, G. R., Welch, C. S., and Munday, J. C.: Wave refraction by warm core rings, Journal of Geophysical Research: Oceans, 90, 7153–7162, 1985.

Marechal, G. and Ardhuin, F.: Surface Currents and Significant Wave Height Gradients: Matching Numerical Models and High-Resolution Altimeter Wave Heights in the Agulhas Current Region, Journal of Geophysical Research: Oceans, 126, e2020JC016 564, 2021.

Mathiesen, M.: Wave refraction by a current whirl, J. Geophys. Res., 92, 3905–3912, 1987.

McWilliams, J. C.: Submesoscale currents in the ocean, 427, 20160 117, https://doi.org/10.1098/rspa.2016.0117, 2016.

Mei, C. C.: Applied dynamics of ocean surface waves, World Scientific, Singapore, second edn., 740 p., 1989.

Monahan, E. C., Spiel, D. E., and Davidson, K. L.: A model of marine aerosol generation via whitecaps and wave disruption, in: Oceanic whitecaps, pp. 167–174, Springer, 1986.

Morrow, R., Fu, L.-L., Ardhuin, F., Benkiran, M., Chapron, B., Cosme, E., D?Ovidio, F., Farrar, J. T., Gille, S. T., Lapeyre, G., Traon, P.-Y. L., Pascual, A., Ponte, A., Qiu, B., Rascle, N., Ubelmann, C., Wang, J., and Zaron, E. D.: Global observations of fine-scale ocean surface topography with the Surface Water and Ocean Topography (SWOT) Mission, 6, 232, https://doi.org/10.3389/fmars.2019.00232, 2019.

Phillips, O. M.: The dynamics of the upper ocean, Cambridge University Press, London, 336 p., 1977.

Quilfen, Y. and Chapron, B.: Ocean Surface Wave-Current Signatures From Satellite Altimeter Measurements, Geophys. Res. Lett., 216, 253–261, https://doi.org/10.1029/2018GL081029, 2019.

Quilfen, Y., Yurovskaya, M., Chapron, B., and Ardhuin, F.: Storm waves sharpening in the Agulhas current: satellite observations and modeling, Remote Sens. Environ., 216, 561–571, https://doi.org/10.1016/j.rse.2018.07.020, 2018.

Rio, M.-H., Mulet, S., and Picot, N.: Beyond GOCE for the ocean circulation estimate: Synergetic use of altimetry, gravimetry, and in situ data provides new insight into geostrophic and Ekman currents, Geophys. Res. Lett., 41, 8918–8925, https://doi.org/10.1002/2014GL061773, 2014.

Rocha, C. B., Chereskin, T. K., and Gille, S. T.: Mesoscale to Submesoscale Wavenumber Spectra in Drake Passage, J. Phys. Oceanogr., 46, 601–620, https://doi.org/10.1175/JPO-D-15-0087.1, 2016.

Romero, L., Lenain, L., and Melville, W. K.: Observations of Surface Wave–Current Interaction, J. Phys. Oceanogr., 47, 615–632, https://doi.org/10.1175/JPO-D-16-0108.1, 2017.

Romero, L., Hypolite, D., and McWilliams, J. C.: Submesoscale current effects on surface waves, Ocean Modelling, 153, 101 662, 2020.

Sandwell, D. T. and Smith, W. H.: Retracking ERS-1 altimeter waveforms for optimal gravity field recovery, Geophysical Journal International, 163, 79–89, 2005.

Shchepetkin, A. F. and McWilliams, J. C.: The regional oceanic modeling system (ROMS): a split-explicit, free-surface, topography-following-coordinate oceanic model, Ocean Modelling, 9, 347–404, https://doi.org/10.1016/j.ocemod.2004.08.002, 2005.

Shchepetkin, A. F. and McWilliams, J. C.: Accurate Boussinesq oceanic modeling with a practical, "Stiffened" Equation of State, Ocean Modelling, 38, 41–70, https://doi.org/10.1016/j.ocemod.2011.01.010, 2011.

Sheres, D., Kenyon, K. E., Bernstein, R. L., and Beardsley, R. C.: Large horizontal surface velocity shears in the ocean obtained from images of refracting swell and in situ moored current data, Journal of Geophysical Research: Oceans, 90, 4943–4950, 1985.

Smit, P. B. and Janssen, T. T.: Swell propagation through submesoscale turbulence, Journal of Physical Oceanography, 49, 2615–2630, 2019.

Tedesco, P., Gula, J., Ménesguen, C., Penven, P., and Krug, M.: Generation of submesoscale frontal eddies in the Agulhas Current, Journal of Geophysical Research: Oceans, 124, 7606–7625, 2019.

The WAVEWATCH III® Development Group: User manual and system documentation of WAVEWATCH III® version 5.16, Tech. Note 329, NOAA/NWS/NCEP/MMAB, College Park, MD, USA, 326 pp. + Appendices, 2016.

Tran, N., Vandemark, D., Labroue, S., Feng, H., Chapron, B., Tolman, H. L., Lambin, J., and Picot, N.: The sea state bias in altimeter sea level
545   estimates determined by combining wave model and satellite data, J. Geophys. Res., 115, C03 020, https://doi.org/10.1029/2009JC005534, 2010.

Villas Bôas, A. B. and Young, W. R.: Integrated observations and modeling of winds, currents, and waves: requirements and challenges for the next decade, J. Fluid Mech., 890, R3, https://doi.org/10.1017/jfm.2020.116, 2020.

Villas Bôas, A. B., Ardhuin, F., Gommenginger, C., Rodriguez, E., Gille, S. T., Cornuelle, B. D., Mazloff, M. R., Bourassa, M., Subrama-
550   nian, A., van Sebille, E., Li, Q., Fox-Kemper, B., Ayet, A., Mouche, A., Merrifield, S. T., Terrill, E. J., Rio, M. H., Brandt, P., Farrar, J. T., Fewings, M., Chapron, B., Shutler, J. D., and Tsamados, M.: Integrated observations and modeling of winds, currents, and waves: requirements and challenges for the next decade, 6, 425, https://doi.org/10.3389/fmars.2019.00425, 2019.

Villas Bôas, A. B., Cornuelle, B. D., Mazloff, M. R., Gille, S. T., and Ardhuin, F.: Wave-Current Interactions at Meso and Submesoscales: Insights fromIdealized Numerical Simulations, J. Phys. Oceanogr., in press, https://doi.org/10.1002/2016JC012413, 2020.

555   White, B. S. and Fornberg, B.: On the chance of freak waves at sea, J. Fluid Mech., 355, 113–138, 1998.

Appendix A: Ray equation in 1D

Let us consider a one dimensional stationary current shear: $\mathbf{u} = (\partial_x U x, 0)$. Starting from the ray equations in a Cartesian frame of coordinate (Mei, 1989; Phillips, 1977):

$$\partial_t k + \partial_x \omega = 0. \tag{A1}$$

560   ω is given by Eq. (2). The time derivative of the wavenumber k is,

$$\partial_t k = -\partial_x \omega. \tag{A2}$$

Considering the intrinsic frequency constant the Eq.(A2) becomes,

$$\partial_t k = -k \partial_x U. \tag{A3}$$

We assume that $\partial_t \omega \sim \partial_t (gk)^{1/2}$. Here we have to derive a function composition. We obtain $\partial_t \sigma = \sqrt{\frac{g}{k}} 2 \partial_t k$. Knowing that
565   the phase speed ($\frac{\omega}{k}$) of waves in deep water is equal to ($\sqrt{\frac{g}{k}}$) it yields:

$$2 \partial_t \sigma = -\sigma \partial_x U. \tag{A4}$$

From Eq.1, assuming stationary condition and that the group speed is much bigger than the current speed

$$\nabla . (\mathbf{C}_g N) = 0 \tag{A5}$$

As $C_g = \frac{1}{2} C_\phi$ with $C_\phi = \sigma/k$, the Eq.A5 becomes,

570    $$\frac{\sigma}{2k\sigma} \frac{E(\sigma)}{\sigma} = Cte. \tag{A6}$$

The constant Cte depends on the initialization of the waves at the left boundary. From Airy theory for waves in deep water combined with Eq.4, one can find that $\frac{H_s^2 g}{4\sigma^2}$=Cte, and so,

$$\frac{H_s}{\sigma} = Cte' \tag{A7}$$

Taking the gradient of the Eq.(A7) combined with Eq.(A1,A3) the constant of Eq.(A7) becomes null and we can write the gradient of the significant wave height as a function of the surface current gradient.

$$\nabla H_s \sim \frac{\partial_x U(H_s k)}{\sigma} \tag{A8}$$